A Deep Learning Approach to Extract Balanced Motions From Sea Surface Height Snapshot

Zhanwen Gao, Bertrand Chapron, Chunyong Ma, Ronan Fablet, Quentin Febvre, Wenxia Zhao, Ge Chen

AGU ADVANCING EARTH AND SPACE SCIENCES

Geophysical Research Letters

RESEARCH LETTER
10.1029/2023GL106623

A Deep Learning Approach to Extract Balanced Motions From Sea Surface Height Snapshot

Zhanwen Gao[1,2], Bertrand Chapron[2], Chunyong Ma[1,3], Ronan Fablet[4], Quentin Febvre[4], Wenxia Zhao[1], and Ge Chen[1,3]

[1]Department of Marine Technology, Ocean University of China, Qingdao, China, [2]Ifremer, UMR CNRS LOPS, Brest, France, [3]Laoshan Laboratory, Qingdao, China, [4]IMT Atlantique, UMR CNRS Lab-STICC, Brest, France

Key Points:

- A Deep learning model is developed to extract balanced motions from sea surface height snapshot based on a realistic simulation
- Diagnostics of three metrics reveal the effectiveness of the model in extracting balanced motions
- The model exhibits remarkable advantages over the Gaussian filter (baseline) in capturing the gradient and Laplacian information

Supporting Information:

Supporting Information may be found in the online version of this article.

Correspondence to:

C. Ma and G. Chen,
chunyongma@ouc.edu.cn;
gechen@ouc.edu.cn

Citation:

Gao, Z., Chapron, B., Ma, C., Fablet, R., Febvre, Q., Zhao, W., & Chen, G. (2024). A deep learning approach to extract balanced motions from sea surface height snapshot. *Geophysical Research Letters*, *51*, e2023GL106623. https://doi.org/10.1029/2023GL106623

Received 28 SEP 2023
Accepted 27 MAR 2024

Abstract Extracting balanced geostrophic motions (BM) from sea surface height (SSH) observations obtained by wide-swath altimetry holds great significance in enhancing our understanding of oceanic dynamic processes at submesoscale wavelength. However, SSH observations derived from wide-swath altimetry are characterized by high spatial resolution while relatively low temporal resolution, thereby posing challenges to extract the BM from a single SSH snapshot. To address this issue, this paper proposes a deep learning model called the BM-UBM Network, which takes an instantaneous SSH snapshot as input and outputs the projection corresponding to the BM. Training experiments are conducted both in the Gulf Stream and South China Sea, and three metrics are considered to diagnose model's outputs. The favorable results highlight the potential capability of the BM-UBM Network to process SSH measurements obtained by wide-swath altimetry.

Plain Language Summary Oceanic dynamic processes can be classified into two categories: balanced geostrophic motions (BM), including large-scale circulation, mesoscale and submesoscale eddy turbulence, and unbalanced wave motions (UBM), including barotropic tides, and inertia–gravity waves (IGWs). Both types of motions coexist and have respective contributions to the sea surface height (SSH). How to extract the BM from the total SSH observations obtained by satellite altimetry is the crucial problem to be solved in this paper. To tackle this issue, we propose a deep learning model named the BM-UBM Network to establish the relationship between the total SSH and the BM component. The BM-UBM Network can generate SSH estimations for the BM when provided with a well-resolved SSH snapshot.

1. Introduction

Conventional nadir-looking satellite altimetry has successfully achieved global sea surface height (SSH) observations with high precision over the past few decades, confirming the fact that our planet earth is dominated by an eddying ocean (Abdalla et al., 2021; Chelton et al., 2011; Chen & Chen, 2023). It is well recognized that mesoscale eddies capture approximately 80% of the total kinetic energy, exerting a significant influence on the ocean circulation, the air-sea interaction, and the marine ecosystem (Dong et al., 2014; Zhang et al., 2014; Zhang & Qiu, 2020). However, the nadir-looking altimeter is limited in its ability to resolve other ocean energetic motions at submesoscale or smaller scales (Amores et al., 2018; Ballarotta et al., 2019; Dufau et al., 2016; Vergara et al., 2019), even though these motions play a crucial role in the cascade and dissipation of ocean energy (Ajayi et al., 2020; Klein et al., 2019; Zhang et al., 2023). To improve the observational capabilities of satellite altimetry, the next generation of wide-swath imaging altimeter has been proposed, including the Surface Water and Ocean Topography (SWOT) satellite launched on 16 December 2022 (Morrow et al., 2019), as well as the Guanlan mission proposed by China (Chen et al., 2019). The unique interferometric techniques improve the measured SSH resolution down to 15–30 km in wavelength (Fu & Ubelmann, 2014; Wang et al., 2019), allowing SWOT to provide the first global SSH observations that encompass multiple ocean motions from mesoscale to submesoscale ranges.

Dynamical oceanic processes captured by wide-swath satellite altimetry include both balanced motions (BM) represented by large-scale circulation, mesoscale and submesoscale turbulences, and unbalanced motions (UBM) represented by barotropic tides and inertia–gravity waves (IGWs) (Torres et al., 2019; Zaron, 2019; Zhang et al., 2019; Zhang & Qiu, 2018). Both types of motions have their projections onto the total SSH and dominate the SSH variability at different spatial scales according to their relative strength. Although SSH observations have been utilized to infer the geostrophic surface currents at large scales, the BM gradually loses its dominance and is overtaken by the UBM as the scale decreases, resulting in failure of geostrophic balance. Therefore, it is necessary

to separate these two types of motions, to reveal their respective characteristics and examine their dynamical interactions.

Several approaches have been proposed to tackle the BM-UBM separation. Richman et al. (2012) used a 48hr cutoff period to delineate the high-frequency components dominated by internal waves and the low-frequency components represented by geostrophic motions. Qiu et al. (2018) and Torres et al. (2018) used spatiotemporal filtering to partition ocean motions into BM and IGWs, where the cutoff frequencies they used are the frequency of either the local tenth vertical-mode IGW dispersion curve or the permissible tides. Wang et al. (2023b) introduced a dynamics-based decomposition, primarily disentangling the BM and UBM by considering the relative magnitudes of the relative vorticity and the modified horizontal divergence in spectral space. Furthermore, Wang et al. (2023a) classified ocean motions into large-scale circulations, barotropic tides, mesoscale (submesoscale) currents, low-mode (high-mode) IGWs based on their respective dynamical characteristics. Contrary to these Eulerian filtering methods mentioned above, Shakespeare et al. (2021) proposed the Lagrangian filtering, which separates the BM from UBM in a frame of reference moving with the flow.

It is worth noting that these methodologies summarized previously require temporally continuous SSH snapshots and therefore are not applicable to wide-swath altimeter satellite which has a long revisit period. The SWOT mission poses the challenge of separating the BM and UBM from a single well-resolved SSH snapshot. Torres et al. (2019) used spatial filtering with the cutoff wavelength (or transition scale) to separate the BM and UBM, and diagnosed the kinetic energy exchanges between them based on SSH snapshots. Le Guillou et al. (2021) introduced a data assimilation technique, named BFN-QG, to map SSH from altimetric observations while respecting quasi-geostrophic dynamics. Additionally, some studies treated the snapshot-style separation of the BM and UBM as an image-to-image translation problem, and used deep learning approaches to solve it. Wang, Grisouard, et al. (2022) used Generative Adversarial Network (GAN) to extract internal tides (IT) from an idealized eddying simulated SSH snapshot. Lguensat et al. (2020) used Residual Network (ResNet) to filter IGWs from SSH data based on a realistic numerical simulation (eNATL60).

The researches of Wang, Grisouard, et al. (2022) and Lguensat et al. (2020) have its own advantages. Wang, Grisouard, et al. (2022) carried out tests under different relative magnitudes of the BM and UBM (by setting different configurations for idealized simulation) in order to mimic various dynamical regimes in the real-ocean scenarios. Lguensat et al. (2020) was an important attempt based on a realistic (rather than idealized) numerical simulation. Therefore, our study combines the advantage of these researches, conducting realistic-simulation-based analysis to extract the BM from SSH snapshot in different oceanic regions representing different dynamical regimes, including the Gulf Stream and South China Sea.

The rest of the paper is organized as follows: Section 2 presents the data set and the decomposition method used in this paper. Section 3 introduces the framework of the BM-UBM Network, including its structure, configurations, results. In Section 4, we discuss some potential limitations of the BM-UBM Network and propose several directions for future work.

2. Data and Method

2.1. MITgcm Numerical Simulation

The data used in this study is the state-of-the-art global ocean simulation from the Massachusetts Institute of Technology general circulation model (MITgcm) with a latitude–longitude–cap (llc) numerical grid (Marshall et al., 1997). The MITgcm llc4320 data set has a 1/48° (~2 km) spatial resolution and a 1h temporal resolution. Not only large-scale circulations, barotropic tides, and mesoscale eddies, but also abundant submesoscale motions, and IGWs have been included in this data set. These realistic ocean simulations are attributed to the surface boundary condition forced by the 6-hourly ERA-Interim atmospheric reanalysis and the synthetic surface pressure field consisting of the full luni-solar tidal potential.

The favorable agreement between the MITgcm llc4320 and in situ observations has been extensively validated. Regarding the BM, Qiu et al. (2018) displayed the agreement of the surface eddy kinetic energy (EKE) estimated from the MITgcm llc4320 and the AVISO SSH product. Regarding the UBM, Savage et al. (2017) showed that the frequency spectrum of the MITgcm llc4320 agreed well with the spectrum derived from the hourly dynamic height measured by nine McLane profiler moorings. Moreover, comparisons between the MITgcm llc4320 and Acoustic Doppler Current Profiler (ADCP) observations has been conducted in many regions, including the

Drake Passage (Rocha, Chereskin, et al., 2016), the North Pacific (Qiu et al., 2017), and the California Ocean Current (Chereskin et al., 2019). Overall, these validation studies highlight the accuracy and reliability of the MITgcm llc4320 in simulating ocean dynamics.

The hourly SSH data of the MITgcm llc4320 from 11 July 2012 to 10 September 2012 are used. The experiments are conducted in two 5° × 5° areas, including the Gulf Stream (38°–43°N, 60°–65°W) and South China Sea (17.5°–22.5°N, 115°–120°E) (Figure S1 in Supporting Information S1). The Gulf Stream (South China Sea) is characterized by stronger BM (UBM) than UBM (BM). Choosing different regions, namely different dynamical regimes, helps demonstrate the usefulness of the BM-UBM Network.

2.2. Balanced–Unbalanced Motions Decomposition

The wavenumber-frequency spectrum of hourly SSH data in the Gulf Stream is plotted in Figure 1a, in which the SSH variance density of the UBM is particularly discernible in the semidiurnal and diurnal tide frequency bands as well as along the dispersion curves of IGWs. Calculation of this wavenumber-frequency spectrum follows the classical methodology also used in Qiu et al. (2018) and Rocha, Gille, et al. (2016). Due to the large horizontal scales of large-scale circulations and barotropic tides ($O(10^3)$km), they have been excluded from the hourly SSH data by removing the mean and linear trend (Wang et al., 2023a), leaving the sea surface height anomaly data used to perform the BM-UBM decomposition. The SSH three-dimensional scalar $T(x,y,t)$ is multiplied by a three-dimensional Hanning window, and we perform a discrete three-dimensional Fourier transform to obtain $\hat{T}(k,l,\omega)$, where k is the zonal wavenumber, l is the meridional wavenumber, and ω is the frequency. Then we need to perform the transformation from an anisotropic spectrum to an isotropic spectrum using the azimuthally-averaged methodology, then obtain the two-dimensional wavenumber-frequency spectrum $S(k_r,\omega)$, where k_r is the isotropic wavenumber defined as $k_r = \sqrt{k^2 + l^2}$. The more detailed calculation process of the azimuthally-averaged methodology can be found in the Text S2 in Supporting Information S1.

The BM-UBM decomposition is conducted in the wavenumber-frequency domain, and the local tenth vertical-mode IGWs dispersion curve (red curve in Figure 1a) is adopted to separate the BM located below this curve and the UBM located above this curve (Torres et al., 2018). To calculate the dispersion curves of IGWs at discrete vertical modes, we first calculate the local buoyancy frequency based on the World Ocean Atlas 2018 (WOA18) climatological temperature–salinity profiles (Zweng et al., 2018). Then, the different Rossby radii of deformation are produced by solving the classical Sturm-Liouville problem (Chelton et al., 1998). Finally, the related dispersion curves of IGWs can be obtained by the function of wavenumber and frequency.

Once the BM and UBM have been separated in the spectral space, an inverse Fourier transform can be applied to reconstruct the BM and UBM in physical space, thereby obtaining their respective projections onto the total SSH. Figures 1b–1d plot the total SSH, the BM and UBM components on 1 September 2012. It is evident that the BM accounts for the majority of the total SSH variation, while the UBM affects the SSH variation at smaller scales. Figure 1j shows the wavenumber spectra of the BM and UBM. Consistent with previous studies, the BM exhibits dominance at mesoscale ranges, while the SSH variance of the UBM surpasses that of the BM at submesoscale ranges (Qiu et al., 2018). The intersection of two power spectral density (PSD) curves corresponds to the transition scale from the BM to UBM. Notably, the wavenumber spectral slope near k^{-5} for the BM are consistent with the predictions of the interior quasi-geostrophic (QG) turbulence theory (Charney, 1971). Additionally, the energy peak in the wavenumber spectrum (around 0.1cpkm) is due to temporal aliasing of IGWs caused by inadequate outputting rate of the MITgcm llc4320 simulation (hourly snapshots) (Wang, Liu, et al., 2022), which leads to the spectral energy of high-frequency (subhourly) IGWs folding back to lower frequencies (as illustrated by the aliased spectral energy of mode-1 IGWs in Figure 1a).

The same decomposition methodology is also applied to separate the BM and UBM from the sea surface velocity data of the MITgcm llc4320 (Figure S2 in Supporting Information S1), and calculate the relative vorticity and horizontal divergence for the decomposition results (Figure S3 in Supporting Information S1). The BM displays mesoscale features as patches with the large relative vorticity and extremely weak horizontal divergence, while the UBM demonstrates a strong horizontal divergence pattern. Therefore, whether the analysis of SSH decomposition results from the perspective of the wavenumber spectrum or the examination of sea surface velocity decomposition results from the perspective of the relative vorticity and horizontal divergence properties, both

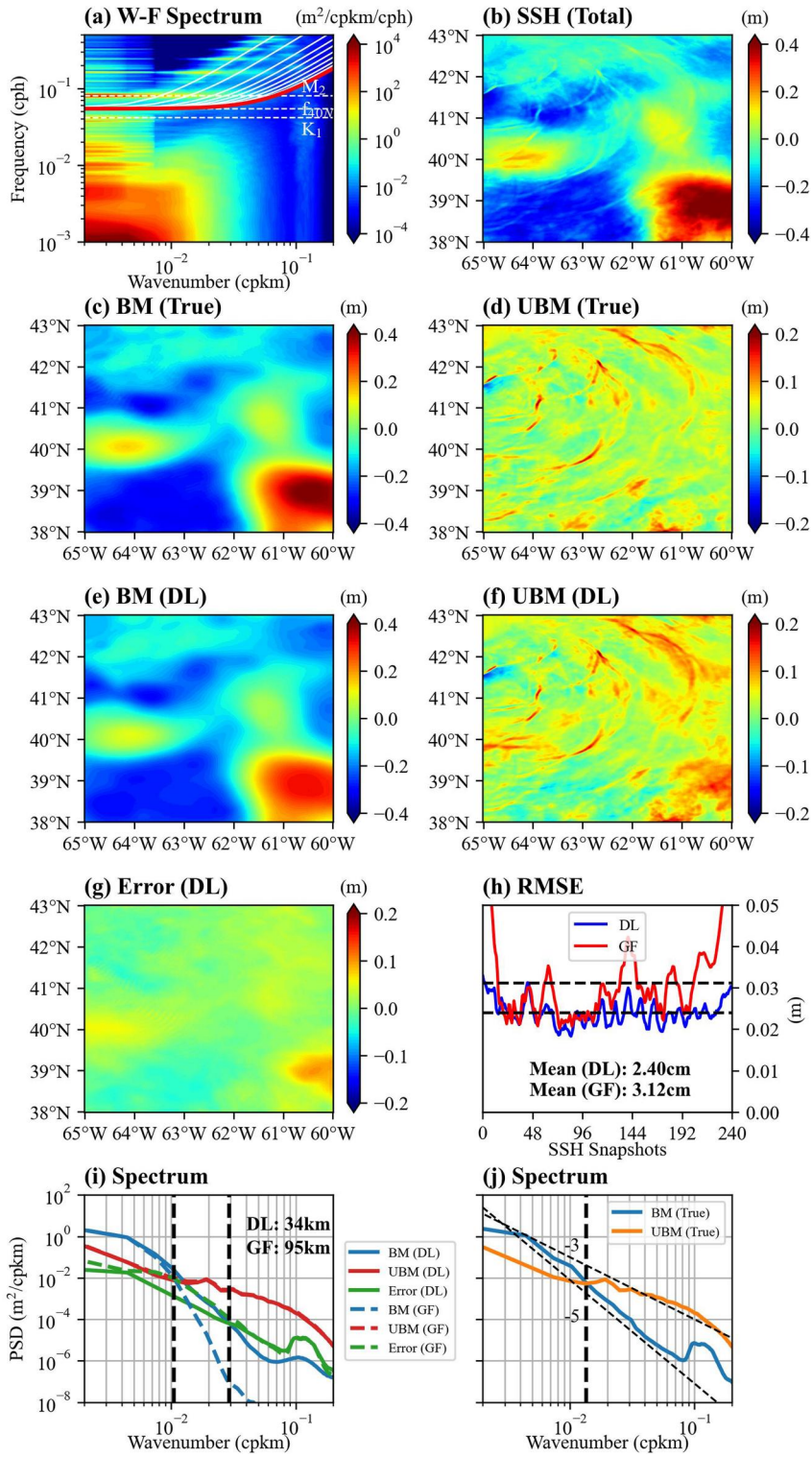

Figure 1.

approaches provide robust evidence to validate the correctness of the decomposition method in separating the BM and UBM components.

3. Deep Learning Framework: BM-UBM Network

3.1. Configurations

The U-Net, a representative of the Convolutional Neural Network (CNN), is particularly suitable for extracting features from one image (Falk et al., 2019). It has been widely used in various oceanographic studies, such as ocean eddies or fronts detection (Liu et al., 2021; Wang, Chen, et al., 2023). In this paper, we propose the BM-UBM Network, which utilizes the U-Net architecture to establish the relationship between the total SSH and its BM component. The network takes the total SSH as input and generates the SSH associated with the BM, and the SSH corresponding to the UBM is obtained by subtracting the BM component from the total SSH. Figure 2 illustrates the architecture of the BM-UBM Network, which consists of an encoder-decoder module and a concatenation module. The encoder module reduces the input image resolution and extracts essential features, whereas the decoder module restores the original resolution of the image to maintain the same resolution between the output and input. Additionally, the concatenation module fuses the encoder and decoder modules at the same level.

Hourly SSH snapshots from MITgcm llc4320 are used as input, and results from the BM-UBM decomposition are used as ground truth. These preprocessed data spanning from July 11 to 21 August 2012, August 22 to 31 August 2012, and September 1 to 10 September 2012 were split into the training/validation/testing data set, respectively. Each SSH snapshot in the testing data set is independently fed into the BM-UBM Network, with the purpose of simulating the BM-UBM Network processing the SWOT-like 2D data. In other words, the BM-UBM Network extracts the BM from the spatial dimension only, independent of the temporal dimension. The training procedure was run on a Nvidia Tesla P100 GPU. The BM-UBM Network was coded using the PyTorch framework and trained using the ADAM optimizer. A supervised learning strategy is used, in which the training loss function involves the mean square error of the SSH and its gradient:

$$\mathcal{L}(x_{\mathrm{SSH}},\tilde{x}_{\mathrm{SSH}}) = \|x_{\mathrm{SSH}} - \tilde{x}_{\mathrm{SSH}}\|^2 + \alpha\|\nabla x_{\mathrm{SSH}} - \nabla\tilde{x}_{\mathrm{SSH}}\|^2 \quad (1)$$

where x_{SSH} is the ground truth from training data set, $\tilde{x}_{\mathrm{SSH}}$ is the prediction from the BM-UBM Network, and α is the weighing parameters whose value is set to 100. The choice of this loss function takes into account both the accuracy of prediction and the preservation of high-frequency information for the SSH field.

3.2. Results

To provide a comparison, we also choose the same moment as an example to show the predicted results of the BM-UBM Network. Comparing the predictions (Figures 1e and 1f) and references (Figures 1c and 1d) of the BM and UBM, it can be concluded that the BM-UBM Network can effectively extract the projection of the BM from the total SSH, and the overall pattern is well described. The UBM results also include detailed SSH information at small scales. Errors between the BM prediction and BM reference are plotted in Figure 1g. Since the UBM prediction is calculated by subtracting the BM prediction from the total SSH, errors between the UBM prediction and the UBM reference have the same values but opposite signs.

Three metrics are considered to diagnose the predicted accuracy of the BM-UBM Network, including (a) the root-mean-square error (RMSE), (b) the wavenumber spectrum, and (c) the wavenumber-frequency spectrum. A total of 240 SSH snapshots are independently processed to ensure that these metrics hold statistical significance. The first RMSE-based metric (blue line in Figure 1h) describes the fluctuation of errors for each SSH snapshot. The

Figure 1. The BM-UBM decomposition results for SSH in the Gulf Stream. (a) The wavenumber-frequency spectrum of hourly SSH data from MITgcm llc4320. Dashed white lines denote the inertial and tidal frequencies. Solid white lines denote the dispersion relation for IGWs of the first 10 vertical modes. Solid red line denotes the frequencies to separate the BM and UBM. (b) An example of the total SSH snapshot. (c) and (d) The decomposition results of the BM and UBM obtained from the wavenumber-frequency spectrum. (e) and (f) The decomposition results of the BM and UBM obtained from the deep learning approach (DL). (g) Error between the BM (DL) and the BM (True). (h) RMS of errors for the DL (blue line) and the Gaussian filter (GF) baseline (red line) over the testing data set, and two black horizontal lines indicate the average values of RMSE. (i) The wavenumber spectra of the BM, UBM, and Error obtained from the DL and GF. Two black vertical lines represent the effective separation scale for the DL and GF, respectively (j) The wavenumber spectra of the BM and UBM, where vertical black dashed line denotes the transition scale from the BM to UBM, and black thin dashed lines denote spectral slopes of k^{-3} and k^{-5} for reference.

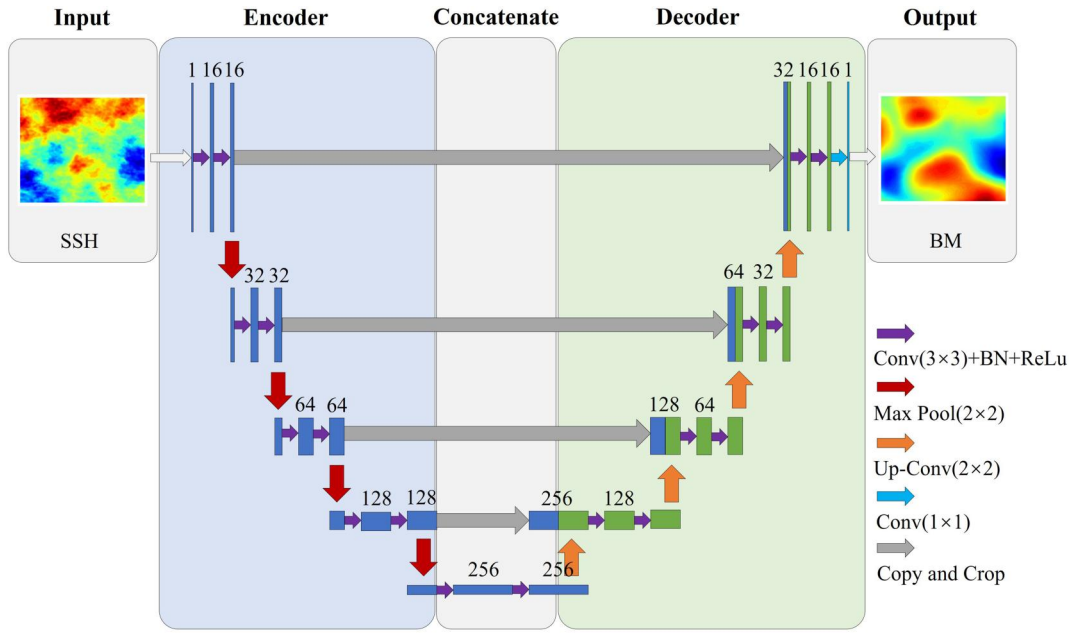

Figure 2. The overall structure of the BM-UBM Network, consisting of the encoder-decoder module and the concatenation module.

variation of RMSE is not significant, consistently ranging within 2–3 cm, with the average RMSE of 2.40 cm. We also calculate the correlation between the BM references and BM predictions, results show that the average correlation coefficient is 0.996 (Figure S4 in Supporting Information S1).

The second metric, wavenumber spectrum, provides a spatial-scale-dependent diagnosis. The zones where the error spectrum is lower than both the BM and UBM will characterize where the separation is effective for both signals. Therefore, the intersection of the error wavenumber spectrum with the BM wavenumber spectrum is defined as the effective separation scale, which is particularly useful to identify the minimum wavelength at which the predicted results are reliable. Results (Figure 1i) show that the effective separation scale of 34 km in the Gulf Stream is roughly consistent with the resolution can be resolved by wide-swath altimetry (15–30 km), which is a robust demonstration of the capability to extract the BM at submesoscale of interest for wide-swath altimetry.

Furthermore, the two-dimensional (2D) Gaussian filter operates on the principle of Gaussian function, which is the most commonly mathematical tool used to smooth data in image processing. It is also adopted as the baseline for comparison with the BM-UBM Network we proposed. The cutoff wavelength of the 2D Gaussian filter is determined by the transition scale between the BM and UBM (Figure 1j). Figure 1h plots errors of the results obtained from the 2D Gaussian filter over the testing data set. The first RMSE-based metric shows that the deep learning approach (DL, blue line in Figure 1h) performs more stable, while the Gaussian filter baseline (GF, red line in Figure 1h) exhibits notable fluctuation of errors for different snapshots, with an average RMSE of 3.12 cm. The second wavenumber spectrum metric reveals an effective separation scale of 95 km for the Gaussian filter (Figure 1i), which is larger than the typical transition scale between the BM and UBM (~74 km, Figure 1j). Such a discrepancy is clearly deemed unacceptable for the BM extraction at submesoscale. Compared to the 2D Gaussian spatial filter, the BM-UBM Network leads to a great improvement with the relative gain of 23% for the RMSE and 64% for the effective separation scale.

The third metric, wavenumber-frequency spectrum, provides a description both in space and time. The wavenumber-frequency spectra of the BM, UBM, error and the ratio of error with both signals are plotted in Figure S5 in Supporting Information S1. The signal-to-noise ratio (SNR) of the BM (Figure S5c in Supporting Information S1) shows that SNR values greater than 1 are concentrated in the low-frequency regions dominated by the BM. Similarly, the SNR of the UBM (Figure S5e in Supporting Information S1) also shows that SNR

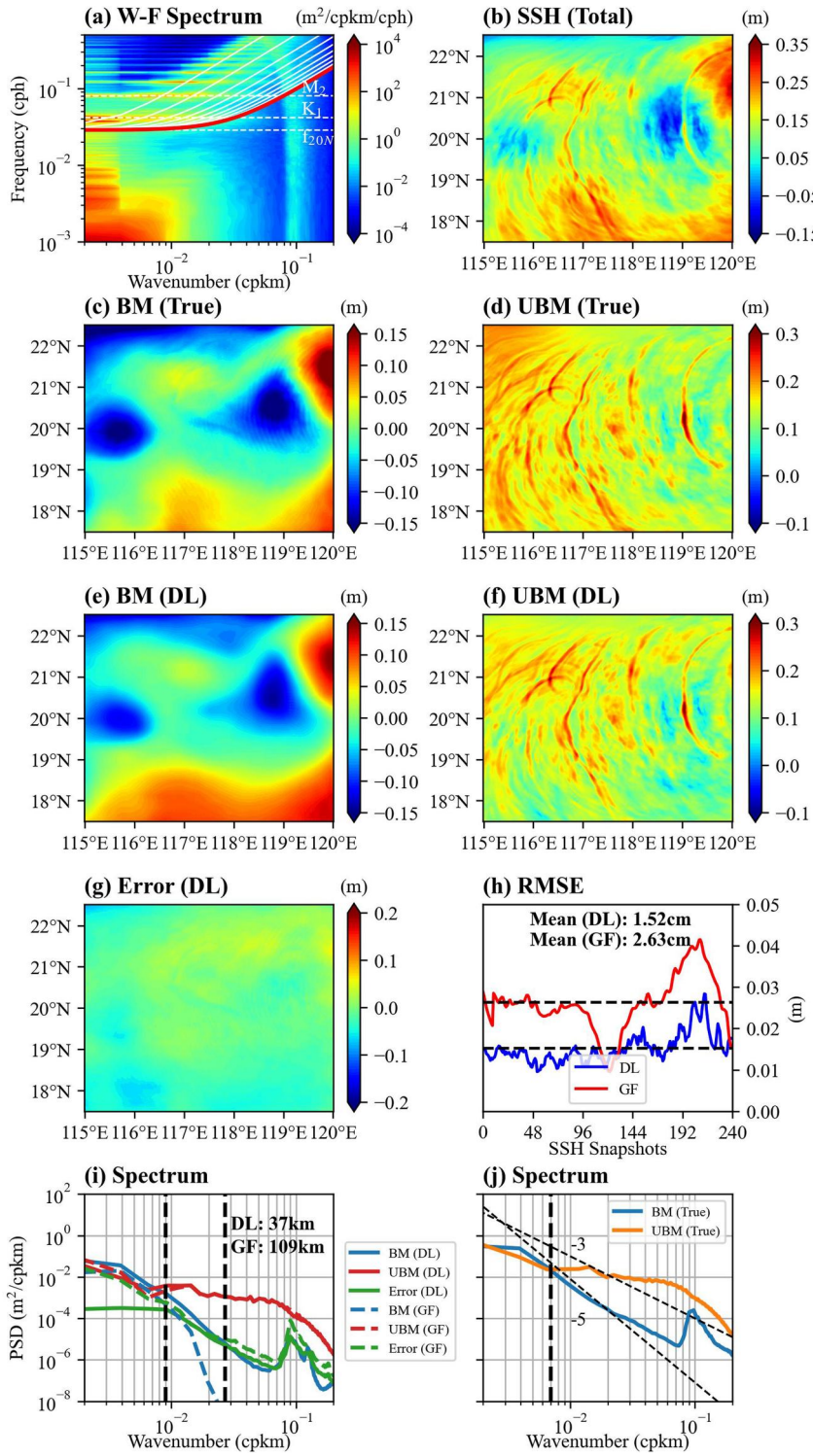

Figure 3. Same as Figure 1 but for the South China Sea.

values greater than 1 are concentrated in the high-frequency regions dominated by the UBM. These results imply that the BM-UBM Network is not only a basic spatial filter, but also has the capability to capture temporal characteristics of ocean dynamics.

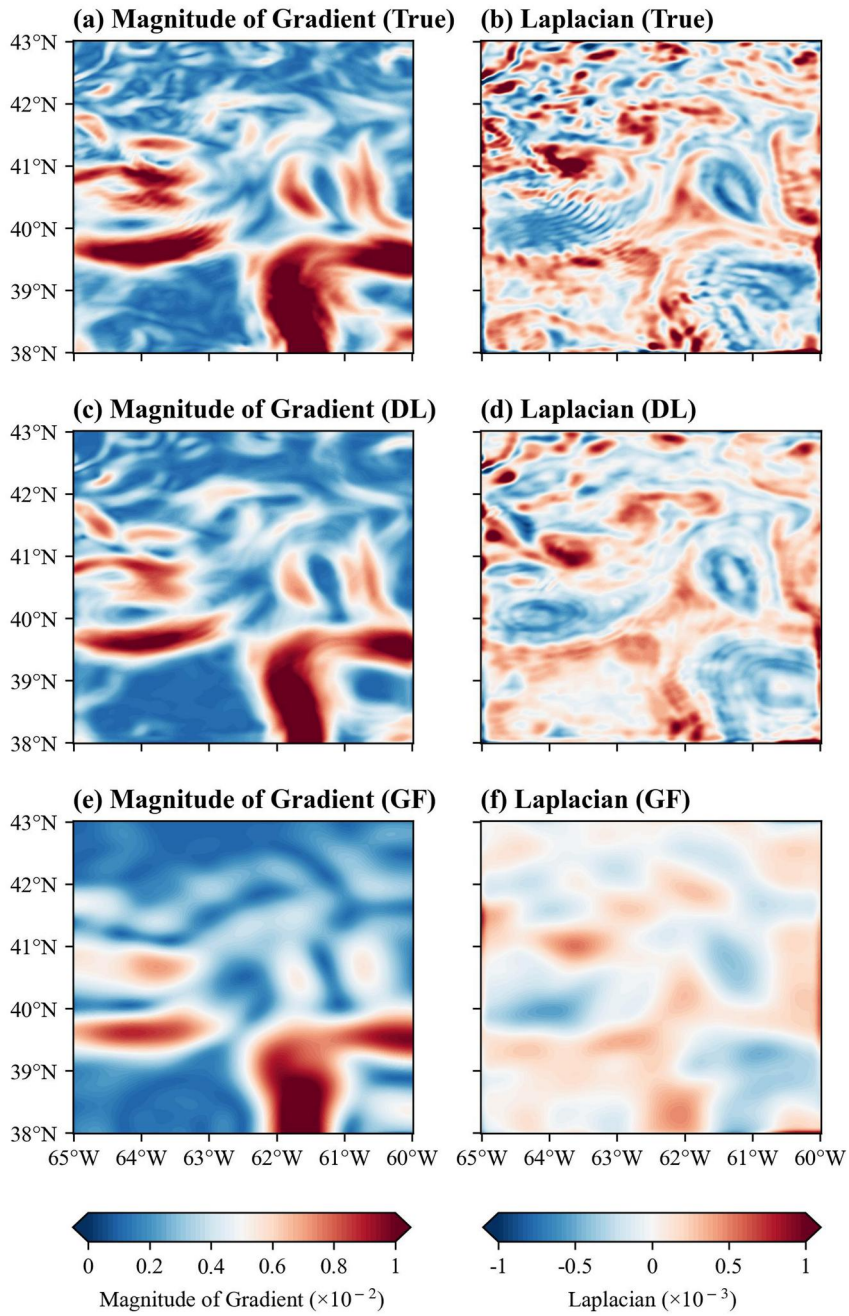

Figure 4. Comparison of the magnitude of the BM gradient and BM Laplacian fields for the True, DL, and GF. Left column is the magnitude of gradient field, and right column is the Laplacian field. Three rows from top to bottom correspond to the BM obtained from the True, DL, and GF, respectively.

To further investigate the performance of the BM-UBM Network under different ocean dynamical regimes, additional analyses are also conducted in a 5° × 5° region within the South China Sea, which is one of the typical representative regions in the global ocean where the UBM is usually stronger than the BM. The UBM has distinct footprints on the total SSH (Figure 3b), with a magnitude greater than that of the BM. The relatively greater strength of the UBM results in a much larger transition scale (~143 km, Figure 3j) than that of the Gulf Stream (~74 km, Figure 1j). The same three metrics are used to evaluate the predicted results obtained from the BM-UBM Network. The average RMSE of 1.52 cm and the effective separation scale of 37 km are better than the 2D Gaussian filter, which has an average RMSE of 2.63 cm and an effective separation scale of 109 km in the

South China Sea. Results of the correlation coefficient and wavenumber-frequency spectrum are plotted in Figures S6 and S7 in Supporting Information S1.

Additionally, we also examine the magnitude of the gradient and Laplacian fields for the BM from the True, DL and GF (Figure 4). The BM outputs from the DL reveal a remarkable consistency with the True both in these two fields. The prominent meanders in the gradient field and numerous vortices in the Laplacian field can be captured by the BM-UBM Network. In contrast, the GF performs significantly worse, and most of the information is smoothed out. This situation is more pronounced for the second-order Laplacian field compared to the first-order gradient field. Although the BM outputs from the GF may appear similar to the True in terms of SSH, it is powerless to capture these two statistical characteristics. Therefore, the robust performance of the BM-UBM Network in capturing features both in the gradient and Laplacian fields is beneficial to utilize SSH to infer geostrophic ocean current based on the QG theory, which is particularly crucial for data analysis of the BM component.

4. Discussion and Outlook

As mentioned in the introduction, oceanic observations cannot give access to a full wavenumber-frequency spectrum. Only a frequency spectrum (such as mooring observations) or a wavenumber spectrum (such as satellite altimeter observations) can be obtained. The poor revisiting cycle of wide-swath altimetry poses challenges to extract the BM from a single SSH snapshot. As a result, we propose a deep learning approach (the BM-UBM Network) as a solution, which takes an instantaneous SSH snapshot as input and generates corresponding projection of the BM. The favorable performance highlights its potential capability to process SSH measurements from wide-swath altimetry. We also expect that the BM-UBM Network will contribute to the study of multiscale oceanic motions in the era of SWOT mission.

It should be acknowledged that the extracted BM could suffer from IGWs leakage and the remaining UBM may also include some leaked submesoscale processes. And the experiment conducted in this paper remain a simulation-based case study, and the BM-UBM Network is also trained to a special region or season. Several studies have already pointed out that the interactions between BM and UBM show large differences in terms of the geographical patterns and seasonality. Qiu et al. (2018) revealed that the dominance of the BM and UBM in SSH variability exhibits significant different characteristics across the global ocean. Not only the geography, we also examine the seasonal modulation by calculating the relative vorticity and horizontal divergence of the sea surface velocity (Figure S8 in Supporting Information S1). Results suggest that the BM is stronger in wintertime, whereas the UBM is more prominent in summertime, consistent with the conclusions of Rocha, Gille, et al. (2016). Therefore, whether the geography or seasonality will be the major challenges in transforming the deep learning method from theoretical analysis to practical tools. Generalization of the BM-UBM Network over the global ocean still deserves great efforts in future work.

Additionally, this paper is mostly a technological demonstration of applying the deep learning method to the BM-UBM decomposition in the context of the fact that deep learning is increasingly widely used in oceanographic researches and more high-spatial resolution SSH measurements will be available from wide-swath altimetry. However, this paper does not provide scientific explanations about why the BM-UBM Network can realize the BM extraction, which may be more confusing to many physical oceanographers who want to seek the physical mechanism behind the BM-UBM Network working. Therefore, advancing the interpretability of deep learning and deepening our understanding of the oceanographic mechanisms are also directions for future work.

As an innovative attempt, the BM-UBM Network is not the final solution and still has numerous areas for improvement. As a natural extension for future research work, we can enhance the BM-UBM Network from the following aspects:

1. Enhancement of network architecture: A more sophisticated network architecture can be used to improve performance. Notably, recent advancements in attention mechanisms, such as channel attention and spatial attention, have demonstrated their applicability in capturing spatial and temporal dependencies (Woo et al., 2018). Therefore, integrating attention mechanisms into the BM-UBM Network could be a promising direction for further enhancement.
2. Incorporation of additional information: Numerous studies have indicated a strong correlation between sea surface temperature (SST) and SSH (Chen et al., 2021; Lguensat et al., 2020). Fablet et al. (2023) emphasize

the contribution of SST-SSH synergies to retrieve a significant fraction of the ageostrophic component. Therefore, introducing additional oceanic variables closely related to the BM and UBM into the BM-UBM Network could potentially improve the decomposition accuracy and provide a more comprehensive understanding of oceanic processes.

3. Testing with measurements from wide-swath altimetry: The current experiment still uses only numerical simulation from the MITgcm llc4320 data set. Further experiments using SSH measurements from wide-swath altimetry can be conducted to display the results obtained from the BM-UBM Network.

Data Availability Statement

The WOA-2018 temperature and salinity gridded data set can be accessed from Locarnini et al. (2018) and Zweng et al. (2018), respectively. The MITgcm llc4320 simulation outputs can be downloaded from ECCO Data Portal (2021). All data sets related to this work are publicly available at Zenodo repository (Gao et al., 2023).

Acknowledgments
This work was supported in part by the National Natural Science Foundation of China under Grant 42276179 and 42030406, in part by Laoshan Laboratory Science and Technology Innovation Projects under Grant LSKJ202201302 and LSKJ202204301, and in part by the Taishan Scholars Program. We thank Dr. Da Liang and Dr. Cesar B. Rocha for providing instructions on the wavenumber-frequency spectrum.

References

Abdalla, S., Kolahchi, A. A., Ablain, M., Adusumilli, S., Bhowmick, S. A., Alou-Font, E., et al. (2021). Altimetry for the future: Building on 25 years of progress. *Advances in Space Research*, *68*(2), 319–363. https://doi.org/10.1016/j.asr.2021.01.022

Ajayi, A., Le Sommer, J., Chassignet, E., Molines, J.-M., Xu, X., Albert, A., & Cosme, E. (2020). Spatial and temporal variability of the North Atlantic eddy field from two kilometric-resolution ocean models. *Journal of Geophysical Research: Oceans*, *125*(5), e2019JC015827. https://doi.org/10.1029/2019JC015827

Amores, A., Jordà, G., Arsouze, T., & Le Sommer, J. (2018). Up to what extent can we characterize ocean eddies using present-day gridded altimetric products? *Journal of Geophysical Research: Oceans*, *123*(10), 7220–7236. https://doi.org/10.1029/2018JC014140

Ballarotta, M., Ubelmann, C., Pujol, M. I., Taburet, G., Fournier, F., Legeais, J. F., et al. (2019). On the resolutions of ocean altimetry maps. *Ocean Science*, *15*(4), 1091–1109. https://doi.org/10.5194/os-15-1091-2019

Charney, J. G. (1971). Geostrophic turbulence. *Journal of the Atmospheric Sciences*, *28*(6), 1087–1095. https://doi.org/10.1175/1520-0469(1971)028<1087:GT>2.0.CO;2

Chelton, D. B., de Szoeke, R. A., Schlax, M. G., El Naggar, K., & Siwertz, N. (1998). Geographical variability of the first baroclinic Rossby radius of deformation. *Journal of Physical Oceanography*, *28*(3), 443–460. https://doi.org/10.1175/1520-0485(1998)028<0433:GVOTFB>2.0.CO;2

Chelton, D. B., Schlax, M. G., & Samelson, R. M. (2011). Global observations of nonlinear mesoscale eddies. *Progress in Oceanography*, *91*(2), 167–216. https://doi.org/10.1016/j.pocean.2011.01.002

Chen, G., Chen, X., & Huang, B. (2021). Independent eddy identification with profiling Argo as calibrated by altimetry. *Journal of Geophysical Research: Oceans*, *126*(1), e2020JC016729. https://doi.org/10.1029/2020JC016729

Chen, G., Tang, J., Zhao, C., Wu, S., Yu, F., Ma, C., et al. (2019). Concept design of the "Guanlan" science mission: China's novel contribution to space oceanography. *Frontiers in Marine Science*, *6*, 194. https://doi.org/10.3389/fmars.2019.00194

Chen, X., & Chen, G. (2023). Quantifying the degree of eddy quasi-geostrophy by generalizing Rossby deformation. *Journal of Geophysical Research: Oceans*, *128*(6), e2023JC019652. https://doi.org/10.1029/2023JC019652

Chereskin, T. K., Rocha, C. B., Gille, S. T., Menemenlis, D., & Passaro, M. (2019). Characterizing the transition from balanced to unbalanced motions in the southern California Current. *Journal of Geophysical Research: Oceans*, *124*(3), 2088–2109. https://doi.org/10.1029/2018JC014583

Dong, C., McWilliams, J. C., Liu, Y., & Chen, D. (2014). Global heat and salt transports by eddy movement. *Nature Communications*, *5*(1), 3294. https://doi.org/10.1038/ncomms4294

Dufau, C., Orsztynowicz, M., Dibarboure, G., Morrow, R., & Le Traon, P. Y. (2016). Mesoscale resolution capability of altimetry: Present and future. *Journal of Geophysical Research: Oceans*, *121*(7), 4910–4927. https://doi.org/10.1002/2015JC010904

ECCO Data Portal. (2021). Estimating the circulation and climate of the ocean (ECCO) [Dataset]. *NASA's Ames Research Center*. Retrieved from https://data.nas.nasa.gov/ecco/

Fablet, R., Febvre, Q., & Chapron, B. (2023). Multimodal 4DVarNets for the reconstruction of sea surface dynamics from SST-SSH synergies. *IEEE Transactions on Geoscience and Remote Sensing*, *61*, 1–14. https://doi.org/10.1109/TGRS.2023.3268006

Falk, T., Mai, D., Bensch, R., Cicek, O., Abdulkadir, A., Marrakchi, Y., et al. (2019). U-Net: Deep learning for cell counting, detection, and morphometry. *Nature Methods*, *16*(1), 67–70. https://doi.org/10.1038/s41592-018-0261-2

Fu, L. L., & Ubelmann, C. (2014). On the transition from profile altimeter to swath altimeter for observing global ocean surface topography. *Journal of Atmospheric and Oceanic Technology*, *31*(2), 560–568. https://doi.org/10.1175/JTECH-D-13-00109.1

Gao, Z., Chapron, B., Ma, C., Fablet, R., Febvre, Q., Zhao, W., et al. (2023). A deep learning approach to extract balanced motions from sea surface height snapshot [Dataset]. *Zenodo*. https://doi.org/10.5281/zenodo.10481076

Klein, P., Lapeyre, G., Siegelman, L., Qiu, B., Fu, L.-L., Torres, H., et al. (2019). Ocean-scale interactions from space. *Earth and Space Science*, *6*(5), 795–817. https://doi.org/10.1029/2018ea000492

Le Guillou, F., Metref, S., Cosme, E., Ubelmann, C., Ballarotta, M., Le Sommer, J., & Verron, J. (2021). Mapping altimetry in the forthcoming swot era by back-and-forth nudging a one-layer quasigeostrophic model. *Journal of Atmospheric and Oceanic Technology*, *38*(4), 697–710. https://doi.org/10.1175/JTECH-D-20-0104.1

Lguensat, R., Fablet, R., Le Sommer, J., Metref, S., Cosme, E., Ouenniche, K., et al. (2020). Filtering internal tides from wide-swath altimeter data using convolutional neural networks. In *In IEEE international geoscience and remote sensing symposium (IGARSS)* (pp. 3904–3907). https://doi.org/10.1109/IGARSS39084.2020.9323531

Liu, Y., Zheng, Q., & Li, X. (2021). Characteristics of global ocean abnormal mesoscale eddies derived from the fusion of sea surface height and temperature data by deep learning. *Geophysical Research Letters*, *48*(17), e2021GL094772. https://doi.org/10.1029/2021GL094772

Locarnini, R. A., Mishonov, A. V., Baranova, O. K., Boyer, T. P., Zweng, M. M., Garcia, H. E., et al. (2018). World ocean atlas 2018, volume 1: Temperature [Dataset]. *NOAA National Centers for Environmental Information*Retrieved from https://www.ncei.noaa.gov/access/world-ocean-atlas-2018/

Marshall, J., Hill, C., Perelman, L., & Adcroft, A. (1997). Hydrostatic, quasi-hydrostatic, and nonhydrostatic ocean modeling. *Journal of Geophysical Research*, *102*(C3), 5733–5752. https://doi.org/10.1029/96JC02776

Morrow, R., Fu, L. L., Ardhuin, F., Benkiran, M., Chapron, B., Cosme, E., et al. (2019). Global observations of fine-scale ocean surface topography with the Surface Water and Ocean Topography (SWOT) mission. *Frontiers in Marine Science*, *6*, 232. https://doi.org/10.3389/fmars.2019.00232

Qiu, B., Chen, S., Klein, P., Wang, J., Torres, H., Fu, L.-L., & Menemenlis, D. (2018). Seasonality in transition scale from balanced tounbalanced motions in the world ocean. *Journal of Physical Oceanography*, *48*(3), 591–605. https://doi.org/10.1175/JPO-D-17-0169.1

Qiu, B., Nakano, T., Chen, S., & Klein, P. (2017). Submesoscale transition from geostrophic flows to internal waves in the northwestern Pacific upper ocean. *Nature Communications*, *8*(1), 14055. https://doi.org/10.1038/ncomms14055

Richman, J. G., Arbic, B. K., Shriver, J. F., Metzger, E. J., & Wallcraft, A. J. (2012). Inferring dynamics from the wavenumber spectra of an eddying global ocean model with embedded tides. *Journal of Geophysical Research*, *117*(C12), C12012. https://doi.org/10.1029/2012JC008364

Rocha, C. B., Chereskin, T. K., Gille, S. T., & Menemenlis, D. (2016a). Mesoscale to submesoscale wavenumber spectra in Drake Passage. *Journal of Physical Oceanography*, *46*(2), 601–620. https://doi.org/10.1175/JPO-D-15-0087.1

Rocha, C. B., Gille, S. T., Chereskin, T. K., & Menemenlis, D. (2016b). Seasonality of submesoscale dynamics in the Kuroshio Extension. *Geophysical Research Letters*, *43*(21), 11304–11311. https://doi.org/10.1002/2016GL071349

Savage, A. C., Arbic, B. K., Alford, M. H., Ansong, J. K., Farrar, J. T., Menemenlis, D., et al. (2017). Spectral decomposition of internal gravity wave sea surface height in global models. *Journal of Geophysical Research: Oceans*, *122*(10), 7803–7821. https://doi.org/10.1002/2017JC013009

Shakespeare, C. J., Gibson, A. H., Hogg, A. M. C., Bachman, S. D., Keating, S. R., & Velzeboer, N. (2021). A new open source implementation of Lagrangian filtering: A method to identify internal waves in high-resolution simulations. *Journal of Advances in Modeling Earth Systems*, *13*(10), e2021MS002616. https://doi.org/10.1029/2021MS002616

Torres, H. S., Klein, P., Menemenlis, D., Qiu, B., Su, Z., Wang, J., et al. (2018). Partitioning ocean motions into balanced motions and internal gravity waves: A modelling study in anticipation of future space missions. *Journal of Geophysical Research: Oceans*, *123*(11), 8084–8105. https://doi.org/10.1029/2018JC014438

Torres, H. S., Klein, P., Siegelman, L., Qiu, B., Chen, S., Ubelmann, C., et al. (2019). Diagnosing ocean-wave-turbulence interactions from space. *Geophysical Research Letters*, *46*(15), 8933–8942. https://doi.org/10.1029/2019GL083675

Vergara, O., Morrow, R., Pujol, I., Dibarboure, G., & Ubelmann, C. (2019). Revised global wave number spectra from recent altimeter observations. *Journal of Geophysical Research: Oceans*, *124*(6), 3523–3537. https://doi.org/10.1029/2018JC014844

Wang, C., Liu, Z., & Lin, H. (2022b). Interpreting consequences of inadequate sampling of oceanic motions. *Limnology and Oceanography Letters*, *7*(5), 385–391. https://doi.org/10.1002/lol2.10260

Wang, C., Liu, Z., & Lin, H. (2023a). On dynamical decomposition of multiscale oceanic motions. *Journal of Advances in Modeling Earth Systems*, *15*(3), e2022MS003556. https://doi.org/10.1029/2022MS003556

Wang, C., Liu, Z., & Lin, H. (2023b). A simple approach for disentangling vortical and wavy motions of oceanic flows. *Journal of Physical Oceanography*, *53*(5), 1237–1249. https://doi.org/10.1175/JPO-D-22-0148.1

Wang, H., Grisouard, N., Salehipour, H., Nuz, A., Poon, M., & Ponte, A. L. (2022). A deep learning approach to extract internal tides scattered by geostrophic turbulence. *Geophysical Research Letters*, *49*(11), e2022GL099400. https://doi.org/10.1029/2022GL099400

Wang, J., Fu, L. L., Torres, H. S., Chen, S., Qiu, B., & Menemenlis, D. (2019). On the spatial scales to be resolved by the surface water and ocean topography Ka-band radar interferometer. *Journal of Atmospheric and Oceanic Technology*, *36*(1), 87–99. https://doi.org/10.1175/JTECH-D-18-0119.1

Wang, Z., Chen, G., Ma, C., & Liu, Y. (2023). Southwestern Atlantic ocean fronts detected from the fusion of multi-source remote sensing data by a deep learning model. *Frontiers in Marine Science*, *10*, 1140645. https://doi.org/10.3389/fmars.2023.1140645

Woo, S., Park, J., Lee, J. Y., & Kweon, I. S. (2018). Cbam: Convolutional block attention module. *Proceedings of the European conference on computer vision (ECCV)*, *11211*, 3–19. https://doi.org/10.1007/978-3-030-01234-2_1

Zaron, E. D. (2019). Baroclinic tidal sea level from exact-repeat mission altimetry. *Journal of Physical Oceanography*, *49*(1), 193–210. https://doi.org/10.1175/JPO-D-18-0127.1

Zhang, Z., Liu, Y., Qiu, B., Luo, Y., Cai, W., Yuan, Q., et al. (2023). Submesoscale inverse energy cascade enhances Southern Ocean eddy heat transport. *Nature Communications*, *14*(1), 1335. https://doi.org/10.1038/s41467-023-36991-2

Zhang, Z., & Qiu, B. (2018). Evolution of submesoscale ageostrophic motions through the life cycle of oceanic mesoscale eddies. *Geophysical Research Letters*, *45*(21), 11847–11855. https://doi.org/10.1029/2018GL080399

Zhang, Z., & Qiu, B. (2020). Surface chlorophyll enhancement in mesoscale eddies by submesoscale spiral bands. *Geophysical Research Letters*, *47*(14), e2020GL088820. https://doi.org/10.1029/2020GL088820

Zhang, Z., Qiu, B., Klein, P., & Travis, S. (2019). The influence of geostrophic strain on oceanic ageostrophic motion and surface chlorophyll. *Nature Communications*, *10*(1), 2838. https://doi.org/10.1038/s41467-019-10883-w

Zhang, Z., Wang, W., & Qiu, B. (2014). Oceanic mass transport by mesoscale eddies. *Science*, *345*(6194), 322–324. https://doi.org/10.1126/science.1252418

Zweng, M. M., Reagan, J. R., Seidov, D., Boyer, T. P., Locarnini, R. A., Garcia, H. E., et al. (2018). World ocean atlas 2018, volume 2: Salinity [Dataset]. *NOAA National Centers for Environmental Information*. Retrieved from https://www.ncei.noaa.gov/access/world-ocean-atlas-2018/